Smart Structures and Systems, *Vol. 33, No. 6 (2024) 431-447*
https://doi.org/10.12989/sss.2024.33.6.431

Acceleration-based fuzzy sliding mode control for high-rise structures with hybrid mass damper

Zhenfeng Lai [1,3], Yanhui Liu*[1,2], Dongfan Ye [1,2], Ping Tan [1,2] and Fulin Zhou [1,3]

[1] *Earthquake Engineering Research & Test Center (EERTC), Guangzhou University, Guangzhou 510006, China*
[2] *Key Laboratory of Earthquake Resistance, Earthquake Mitigation and Structural Safety, Ministry of Education, Guangzhou 510006, China*
[3] *Guangdong Provincial Key Laboratory of Earthquake Engineering and Applied Technology, Guangzhou 510006, China*

(*Received February 16, 2023, Revised September 30, 2023, Accepted November 10, 2023*)

Abstract. The Hybrid Mass Damper (HMD) has proven effective in mitigating vibrations in high-rise structures subject to seismic and wind-induced excitations. One derivative configuration of the HMD mounts an Active Mass Damper (AMD) atop a Tuned Mass Damper (TMD). However, the control efficacy of such HMDs may be compromised when confronted with loads that exceed their design parameters. Additionally, the confined structural space within high-rise structures often limits the feasibility and economic viability of retrofitting HMD systems. This study introduces an Acceleration-based Fuzzy Power Approach Rate Sliding Mode Control (AFP-SMC) algorithm aimed at enhancing the control efficacy of HMDs while minimizing their stroke and force output requirements. Employing the Canton Tower as a research prototype, an analytical model incorporating HMDs was established, and a comparative analysis between the AFP-SMC and Linear Quadratic Gaussian (LQG) control algorithms was conducted for efficacy. The control performance of the AFP-SMC control algorithm under different control parameter variations was investigated. Furthermore, by experimentally assessing the AMD subsystem within the Canton Tower, friction and ripple force formulas were derived to bolster the analytical model, thereby validating the robustness of the AFP-SMC algorithm. The results show that the proposed AFP-SMC algorithm effectively reduces the vibration response of the structure and the stroke and control force output of HMDs, and exhibits superior overall control performance and robustness compared to the LQG algorithm.

Keywords: fuzzy control; hybrid mass damper; LQG; sliding mode control; vibration control

1. Introduction

Mitigating detrimental responses in building structures under various types of loading, such as earthquakes and winds, remains a critical area of research in civil engineering. Advances in structural control methods have yielded various techniques that generally fall into four primary categories: passive, semi-active, active, and hybrid control systems (Ohtori *et al*. 2004). Tuned mass dampers (TMDs) and active mass dampers (AMDs) are prevalent methods for vibration control (Rana and Soong 1998, Sladek and Klinger 1983). For instance, Zou *et al*. (2020) presented a TMD system designed for the bi-directional vibration suppression of offshore wind turbines, validating its performance through numerical simulations. Similarly, Yamamoto and Sone (2014) explored the energy efficiency and vibration control effectiveness of a 24-story building equipped with an AMD, showing that the energy-regenerative system reduced energy consumption. However, TMDs exhibit vulnerabilities, including a high sensitivity to frequency deviations and challenges in frequency adjustment (Esteki *et al*. 2015). In active control systems, the failure of sensors or actuators, or interruptions in external energy supply, can lead to a complete loss of control effectiveness. Additionally, active control systems necessitate robust and stable strategies due to their reliance on sensors and actuators.

The commonly used hybrid mass damper (HMD) typically refers to an active-controlled tuned mass damper (ATMD), which entails a connection between the actuator and the TMD (Koutsoloukas *et al*. 2022). Previous studies have investigated the use of HMD systems in various contexts. For instance, Nagashima *et al*. (2001) employed an HMD system for vibration control in a 36-story biaxial eccentric high-rise building in Tokyo. Similarly, Mamat *et al*. (2018) examined the application of HMDs in high-rise structures, focusing on vibration control analysis and the development of appropriate control strategies. Another configuration of the HMD, also known as DUOX, involves mounting an AMD at the top of a TMD, and the mass of the AMD constitutes approximately 10%-15% of the mass of the TMD. (Sakamoto and Kobori 1995). This particular HMD configuration allows for the simultaneous utilization of both the control features of the TMD and AMD; even if the AMD fails, the TMD component still serves the control function. Notably, such HMD systems have been successfully installed in Japan's Ando Nishikicho Building and the Dowa Kasai Phoenix Tower, remaining operational even during major seismic events (Nishitani 1998). The Canton Tower also employs this type of HMD, which has

*Corresponding author, Ph.D., Professor,
E-mail: liuyanhui2012@163.com

ISSN: 1738-1584 (Print), 1738-1991 (Online)

repeatedly ensured the structural safety of the tower under typhoon conditions. However, in such HMD configurations, the mass and volume of the TMD are often considerable. This poses particular challenges in the confined spaces of high-rise buildings, where external loads may cause the control force and stroke of HMD to exceed acceptable limits, thus compromising control effectiveness. Therefore, HMDs require further research, refinement, and more advanced control strategies to enhance their performance. This type of HMD (i.e., DUOX) is also used in this study and will be referred to as HMD throughout the remainder.

In the realm of structural vibration control for large buildings, multiple interfering and uncertain variables can compromise the accuracy or effectiveness of control systems, sometimes leading to outright failure. Ensuring a reliable control algorithm thus becomes one of the pivotal aspects of structural control. Within this context, the Linear Quadratic Regulator (LQR) has emerged as a classic method for full-state feedback control (Khansefid and Bakhshi 2019, Ho and Ma 2007). Extensive research efforts have been undertaken to optimize the LQR weight matrix for enhancing control performance (Miyamoto *et al*. 2018, Shi *et al*. 2014). Nevertheless, achieving full-state feedback in large building structures proves both challenging and costly, giving rise to the popularity of the Linear Quadratic Gaussian (LQG) control algorithm (Kumar *et al*. 2023, You *et al*. 2014). For instance, Wu and Yang (2000) employed an LQG control strategy using acceleration feedback to reduce the response of the Nanjing TV transmission tower, demonstrating its efficacy in mitigating lateral-torsional coupling motion.

Among the various active control algorithms reported in the literature, sliding mode control (SMC) is a nonlinear active control algorithm that has been continuously improved throughout the 20th century. Yang *et al*. (1995) took the lead in introducing the SMC method into the vibration control of civil engineering structures. They designed a control law using the Lyapunov direct method. SMC algorithm has since been extensively applied for minimizing the impact of both earthquake and wind-induced forces on structures under horizontal loads (Thenozhi and Yu 2013, Fallah and Taghikhany 2015, Yakut and Alli 2011). Although SMC offers robust resilience against external and internal disturbances, chattering remains a major drawback of the traditional SMC algorithm (Concha *et al*. 2021, Xiao *et al*. 2022). To address this, fuzzy control methods have been introduced (Ghaffarzadeh and Aghabalaei 2017, Baghaei *et al*. 2019, Alli and Yakut 2005), offering advantages in systems with imprecise or uncertain variables, often outperforming traditional control algorithms.

In the design of structural control algorithms, multiple factors come into play, including the intrinsic properties of the structure, the external forces it experiences, predefined control objectives, and the range of available control devices. To effectively minimize the vibrational response of the structure, the performance of damping control devices (such as TMD and HMD) should also be considered, especially in the limited space of high-rise building structures, the operation of the control devices in space should also be considered to avoid exceeding the design limits. This study proposes an Acceleration-based Fuzzy Power Approach Rate SMC (AFP-SMC) algorithm, aimed at reducing both the vibrational response of high-rise structures and the stroke and control force exerted by the HMD. Firstly, a switching function is designed to determine the switching surface. Then, the power reaching law is used to design the controller, and the weight matrix is optimized using a genetic algorithm. Utilizing the Canton Tower, equipped with an HMD, as a research prototype, an analytical model was established. Subsequent simulations were conducted to compare the performance of the proposed AFP-SMC algorithm with the LQG algorithm under three distinct wind loading scenarios, as well as to evaluate the efficacy of AFP-SMC across different control parameters. In addition, to further verify the robustness of the AFP-SMC algorithm, the dynamic performance of the AMD subsystem in the Canton Tower is tested, and the friction and ripple thrust formula of AMD are proposed and introduced into the analysis model for simulation research. The results show that the proposed AFP-SMC algorithm is superior to the LQG algorithm, and reduces the stroke and control force of HMD.

The remainder of this paper is structured as follows. In Section 2, the design of the AFP-SMC algorithm is presented. The model construction and numerical simulations of Canton Tower are presented in Section 3. In Section 4, results regarding the robustness of AFP-SCM under different disturbance factors are presented. Finally, the conclusions are summarized in Section 5.

2. Design of AFP-SMC algorithm

The state–space equation of a general control system can be expressed as follows

$$\begin{cases} \dot{\mathbf{Z}} = \mathbf{AZ} + \mathbf{BU} \\ \mathbf{Y} = \mathbf{GZ} + \mathbf{DU} \end{cases} \tag{1}$$

where **A**, **B**, **G** and **D** signify the state, input, output, and transmission matrices, respectively. **Z**, **U** and **Y** represent the state of the system, input, and output vectors, respectively.

In Fig. 1, the system state **Z** is divided into two parts (i.e., $S > 0$ and $S < 0$) by the switching surface $S(Z) = 0$. Points A, B, and C represent an arbitrary state, the initial state, and the terminal state, respectively. The goal of the controller is typically to make the system state start from the initial point B, undergo sliding motion in the sliding mode region, and eventually converge to the terminal point C.

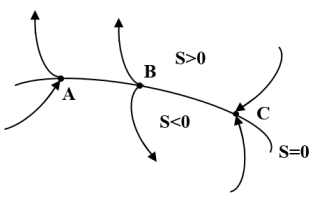

Fig. 1 Sliding surface

When the point is proximity the switching surface S(**Z**) = 0, the conditions $\lim_{S\to 0^+}\dot{S}\le 0$ and $\lim_{S\to 0^-}\dot{S}\ge 0$ (i.e., $\lim_{S\to 0}S\dot{S}\le 0$) hold true. In such a case, the following Lyapunov function is considered

$$V(\mathbf{Z})=\frac{1}{2}S^2(\mathbf{Z}) \tag{2}$$

By differentiating Eq. (2) and allowing the limit of S(Z) to approach 0, it becomes evident that the derivative is non-positive, confirming the decreasing nature of the function. Consequently, sliding mode control can be distilled into two problems:

1. Formulate a switching function that satisfies $\lim_{S\to 0}S\dot{S}\le 0$;
2. Construct a controller that facilitates the sliding of state points on the switching surface.

2.1 Design of switching function

A switching surface is constructed using the state-space equation Eq. (1) of the control system and disregarding the impact of noise, as shown in Eq. (3). The dimensions of S are identical to those of the system state vector.

$$S(\mathbf{Z})=\boldsymbol{\Theta}\mathbf{Z}=0 \tag{3}$$

To determine the matrix **Θ,** the following equation transformations and constructions are performed. Specifically, the system state **Z** is transformed to satisfy the following expression

$$\boldsymbol{\eta}=\boldsymbol{\Gamma}\mathbf{Z} \tag{4}$$

where the is $\boldsymbol{\Gamma}$ an invertible matrix.

By substituting Eq. (4) into Eq. (3) and ignoring the effects of noise and external excitation, the state equation and switching surface expressed in terms of $\boldsymbol{\eta}$ can be obtained as follows

$$\dot{\boldsymbol{\eta}}=\bar{\mathbf{A}}\boldsymbol{\eta}+\bar{\mathbf{B}}\mathbf{U} \tag{5}$$

$$S=\bar{\boldsymbol{\Theta}}\boldsymbol{\eta}=0 \tag{6}$$

where $\bar{\mathbf{A}}=\Gamma\mathbf{A}\Gamma^{-1}$, $\bar{\mathbf{B}}=\boldsymbol{\Gamma}\mathbf{B}$, and $\bar{\boldsymbol{\Theta}}=\boldsymbol{\Theta}\boldsymbol{\Gamma}^{-1}$, and the matrices are partitioned to facilitate expression and computation, as shown in Eq. (7). The dimensions of each block matrix or vector in the equation are determined by the number of controllers. In this study, $\boldsymbol{\eta}_2$ denotes a 1-dimensional vector.

$$\boldsymbol{\eta}=\begin{bmatrix}\boldsymbol{\eta}_1\\ \boldsymbol{\eta}_2\end{bmatrix},\quad \bar{\mathbf{A}}=\begin{bmatrix}\bar{\mathbf{A}}_{11} & \bar{\mathbf{A}}_{12}\\ \bar{\mathbf{A}}_{21} & \bar{\mathbf{A}}_{22}\end{bmatrix},\quad \bar{\boldsymbol{\Theta}}=[\bar{\boldsymbol{\Theta}}_1 \quad \bar{\boldsymbol{\Theta}}_2] \tag{7}$$

Building upon the three aforementioned Eqs. (5)-(7), the validity of the following equations is postulated

$$\dot{\boldsymbol{\eta}}_1=\bar{\mathbf{A}}_{11}\boldsymbol{\eta}_1+\bar{\mathbf{A}}_{12}\boldsymbol{\eta}_2 \tag{8}$$

$$S=\bar{\boldsymbol{\Theta}}_1\boldsymbol{\eta}_1+\bar{\boldsymbol{\Theta}}_2\boldsymbol{\eta}_2=0 \tag{9}$$

The matrix $\boldsymbol{\Gamma}$ is subsequently solved using the Singular Value Decomposition (SVD) method based on Eqs. (8) and (9). SVD is defined as the existence of an m-order matrix $\boldsymbol{\varphi}$ and an n-order matrix $\boldsymbol{\sigma}$, such that the matrix **T** satisfies the following expression

$$\mathbf{T}=\boldsymbol{\varphi}\cdot\boldsymbol{\sigma}\cdot\mathbf{V}^{\mathrm{T}} \tag{10}$$

where **T** is the matrix to be decomposed, $\boldsymbol{\varphi}$ and **V** are two orthogonal matrices, and $\boldsymbol{\sigma}$ is a diagonal matrix with non-negative real numbers.

After solving for $\boldsymbol{\varphi}$, it is divided into blocks, as expressed in Eq. (11). In this study, $\boldsymbol{\varphi}_2$ denotes a 1-dimensional vector and Eq. (11) is used for position transformation, as defined by Eq. (12).

$$\boldsymbol{\varphi}=[\boldsymbol{\varphi}_1,\boldsymbol{\varphi}_2]^{\mathrm{T}} \tag{11}$$

$$\bar{\boldsymbol{\varphi}}=[\boldsymbol{\varphi}_2,\boldsymbol{\varphi}_1]^{\mathrm{T}} \tag{12}$$

$\boldsymbol{\Gamma}$ is defined as $\boldsymbol{\Gamma}=\bar{\boldsymbol{\varphi}}^{-1}$, such that $\bar{\mathbf{B}}=\boldsymbol{\Gamma}\mathbf{B}$ satisfies Eqs. (5) and (6). By defining $\bar{\boldsymbol{\Theta}}_2$ as a unit vector, the following equation can be obtained

$$\boldsymbol{\eta}_2=-\bar{\boldsymbol{\Theta}}_1\boldsymbol{\eta}_1 \tag{13}$$

$$\dot{\boldsymbol{\eta}}_1=(\bar{\mathbf{A}}_{11}-\bar{\mathbf{A}}_{12}\bar{\boldsymbol{\Theta}}_1)\boldsymbol{\eta}_1 \tag{14}$$

In this study, assuming the objective function is defined as Eq. (15).

$$J=\int_0^{\mathrm{t}}[\mathbf{Z}^{\mathrm{T}}\mathbf{Q}\mathbf{Z}]\,dt \tag{15}$$

where **Q** is a positive-definite weight matrix. By taking the Eq. (4) into Eq. (15), Eq. (16) is obtained. For the sake of convenience in expression and computation, the weight matrix **Q** is transformed and partitioned as shown in Eq. (17). Eq. (16) is derived and solved, and $\boldsymbol{\eta}_1$ is considered the variable of $\boldsymbol{\eta}_2$ to obtain Eq. (18).

$$J=\int_0^{t}[\boldsymbol{\eta}^{\mathrm{T}}(\boldsymbol{\Gamma}^{-1})^{\mathrm{T}}\mathbf{Q}(\boldsymbol{\Gamma}^{-1})\boldsymbol{\eta}]\,dt \tag{16}$$

$$\bar{\mathbf{Q}}=(\boldsymbol{\Gamma}^{-1})^{\mathrm{T}}\mathbf{Q}(\boldsymbol{\Gamma}^{-1})=\begin{bmatrix}\bar{\mathbf{Q}}_{11} & \bar{\mathbf{Q}}_{12}\\ \bar{\mathbf{Q}}_{21} & \bar{\mathbf{Q}}_{22}\end{bmatrix} \tag{17}$$

To minimize the objective function represented by Eq. (16), the equation is differentiated and solved, while $\boldsymbol{\eta}_1$ is taken as a variable of $\boldsymbol{\eta}_2$, as shown in the following equation.

$$\boldsymbol{\eta}_2=-\frac{1}{2}\bar{\mathbf{Q}}_{22}^{-1}(\bar{\mathbf{A}}_{12}^{\mathrm{T}}\mathbf{P}+2\bar{\mathbf{Q}}_{21})\boldsymbol{\eta}_1 \tag{18}$$

where **P** is the solution to the Riccati equation in Eq. (19), and $\hat{\mathbf{A}}$ is expressed as Eq. (20).

$$\hat{\mathbf{A}}^{\mathbf{T}}\mathbf{P}+\mathbf{P}\hat{\mathbf{A}}-\frac{1}{2}\mathbf{P}\bar{\mathbf{A}}_{12}\bar{\mathbf{Q}}_{22}^{-1}\bar{\mathbf{A}}_{12}^{\mathrm{T}}\mathbf{P}+2(\bar{\mathbf{Q}}_{11}-\bar{\mathbf{Q}}_{12}\bar{\mathbf{Q}}_{22}^{-1}\bar{\mathbf{Q}}_{12}^{\mathrm{T}})=0 \tag{19}$$

$$\widehat{\mathbf{A}} = \overline{\mathbf{A}}_{11} - \overline{\mathbf{A}}_{11}\overline{\mathbf{Q}}_{22}^{-1}\overline{\mathbf{Q}}_{21} \tag{20}$$

Eq. (21) is obtained by combining Eq. (19) with Eq. (9). Based on this equation, the matrix can be calculated to determine the switching surface.

$$\begin{cases} \overline{\mathbf{\Theta}}_1 = \dfrac{1}{2}\overline{\mathbf{Q}}_{22}^{-1}(\overline{\mathbf{A}}_{12}^{\mathrm{T}}\mathbf{P} + 2\overline{\mathbf{Q}}_{21}) \\ \mathbf{\Theta} = \overline{\mathbf{\Theta}}\mathbf{\Gamma} = [\overline{\mathbf{\Theta}}_1, \mathbf{I}]\mathbf{\Gamma} \end{cases} \tag{21}$$

2.2 Controller design

The primary objective in designing a sliding mode controller is to guide the system state towards a predetermined sliding surface, ensuring it remains on this surface. Factors, such as the controlled object and specific control tasks, heavily influence the design of the controller. In this study, the power reaching law is used to design the sliding mode controller. This law provides an algorithmic description of the convergence rate of the system state, determining the rate according to the deviation of the state from the switching surface. The expression for calculating the control force based on the power reaching law is as follows

$$\mathbf{U} = -(\mathbf{\Theta B})^{-1}[\mathbf{\Theta AZ} + \mathbf{L}f(S)] \tag{22}$$

$$\begin{cases} f(\mathrm{S}) = [f(\mathrm{S}_1), f(\mathrm{S}_2), f(\mathrm{S}_3), \cdots f(\mathrm{S}_\mathrm{r})] \\ f(\mathrm{S}_\mathrm{i}) = |\mathrm{S}_i|^{\alpha}\mathrm{sgn}(\mathrm{S}_i) \end{cases} \quad i = 1,2,3 \ldots \tag{23}$$

where S_i represents the i-th element on the switching surface, with the total number of elements corresponding to the control force outputs. sgn is a symbolic function, while $\mathbf{L}$ is a diagonal matrix; The coefficient α adjusts system deviations, and r signifies the number of control devices.

For the system state to rapidly converge to its designed state, especially when distant from the sliding mode switching surface, and to ensure a slower approach speed when near the surface, judicious parameter selection becomes imperative. This study employed a fuzzy controller to adjust the parameter α, allowing for adaptive dynamic parameter adjustment within the range of 0 to 3 based on changes in structural response.

2.2.1 Fuzzy control algorithm for SMC controller

In this study, acceleration is a key control indicator because it can help achieve a faster control response. To align with control objectives, the displacement-related term in the sliding surface S and the acceleration-related term in its derivative dS are taken as fuzzy control input variables. The output variable, denoted as ε, corresponds to the parameter α. By integrating Eqs. (22) and (23), the control

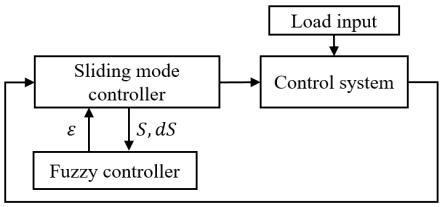

Fig. 2 Control system

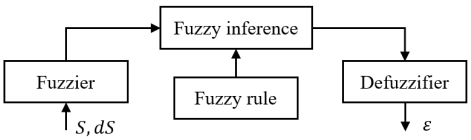

Fig. 3 Fuzzy controller

Table 1 Fuzzy control rules

	ε	dS				
		NB	NS	ZO	PS	PB
S	NB	PB	PB	PS	ZO	ZO
	NS	PB	PS	ZO	ZO	ZO
	ZO	PS	ZO	ZO	ZO	PS
	PS	ZO	ZO	ZO	PS	PB
	PB	ZO	ZO	PS	PB	PB

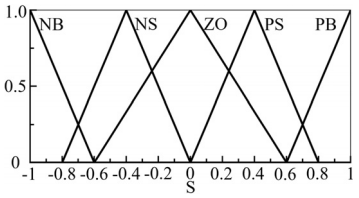

(a) Input variable S

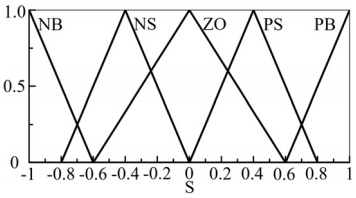

(b) Input variable dS

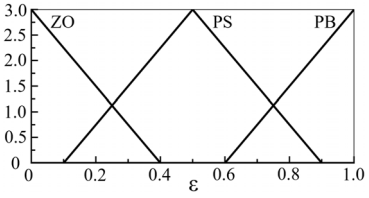

(c) Output variable ε

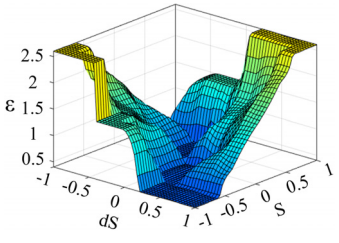

(d) Schematic diagram of fuzzy rules

Fig. 4 Membership function value and fuzzy rules

force Eq. (24) with ε as the fuzzy output variable can be derived. Fig. 2 illustrates a diagram of the fuzzy SMC system, while the fuzzy controller is depicted in Fig. 3. Considering the design of the sliding mode surface, as well as the response features of the system and stability requirements, the triangular membership function was selected. This selection offers computational simplicity while satisfying the aforementioned criteria. Figs. 4(a)-(c) display the preset values for the membership function of both input and output variables. The fuzzy input variables underwent normalization to ensure their values in the fuzzy domain ranged from -1 to 1.

To define the fuzzy rules of the input and output variables, the fuzzy subset {NB, NS, ZO, PS, PB} was used to describe the linguistic values of the input fuzzy variables, whereas the fuzzy subset {ZO, PS, PB} was used to describe the linguistic values of the output fuzzy variables. NB and NS represent negative large and negative small, respectively. ZO is indicative of zero, while PB and PS denote positive large and positive small values, respectively. Table 1 lists the fuzzy control rules that dictate the relationship between input and output, and Fig. 4(d) provides a visual representation of this relationship.

In this section, a sliding surface and an objective function are designed, and a fuzzy controller is integrated with the previously established sliding mode controller. It is proposed that the displacement-related term of the sliding mode surface and the acceleration-related term in its derivative be used as input variables for the fuzzy controller, with the parameter α designated as the output. Fuzzy rules are then formulated based on these variables. This configuration is designed to enhance the control performance of the sliding mode controller.

$$\mathbf{U} = -(\mathbf{\Theta B})^{-1}[\mathbf{\Theta AZ} + \mathbf{L}|\mathrm{S}|^{\varepsilon}\mathrm{sgn}(\mathrm{S})] \tag{24}$$

3. Numerical simulation analysis based on Canton Tower

3.1 Introduction of Canton Tower

Canton Tower, which is 600 m high, is used for broadcasting and sightseeing and includes a 450-m-high main tower and 150-m-high mast (see Fig. 5(a)). To mitigate the effects of wind-induced vibrations, two HMDs (i.e., DUOXs) were installed at a height of 438.4 m with respect to the main tower. Each HMD consisted of a TMD and an AMD. The AMD, which was driven by four linear motors, was mounted on top of the TMD, as shown in Fig. 5(b). The TMD was composed of a fire water tank, and the weight of the water tank was 5880 kN under full water conditions. Each linear motor was capable of producing a rated control force output of 8 kN, with a maximum output of 18kN. The rated force output of each AMD was 32 kN, and the maximum output was 72 kN. The weight of the AMD was 568.4 kN, and the maximum speed was limited to 0.5 m/s.

3.1.1 Analysis model of the Canton Tower

The tower was initially modeled using the finite element method in 3D with ANSYS software (The ANSYS Inc., Pittsburgh, Pennsylvania, USA), as depicted in Fig. 5(b). To simplify calculation and analysis, a multi-degree-of-freedom (MDOF) analysis model was derived from the 3D finite element model using the following steps:

(1) The mass matrix was derived as a diagonal matrix, by concentrating the mass of the tower into the corresponding 51 node layers, including the weight of both structural and non-structural members and the live load. A total of 153 degrees of freedom were considered, with three degrees of freedom in each node layer in three directions (two horizontal and one rotation around the vertical axis).

(2) The stiffness matrix was determined using the flexibility method applied to the 3D ANSYS finite element model.

(3) For practical engineering systems, the damping coefficient matrix cannot be directly calculated. In this

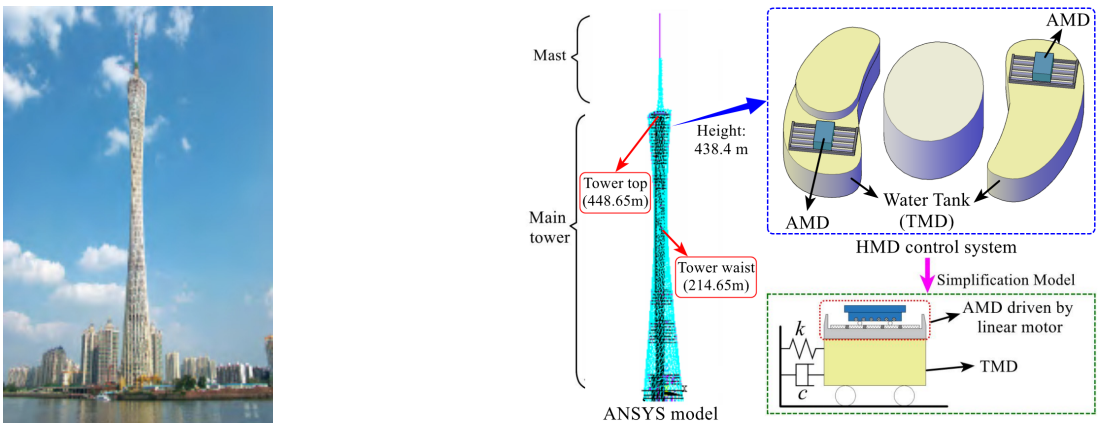

(a) Canton Tower

(b) ANSYS model and HMDs system

Fig. 5 Canton Tower and analysis model

study, the Rayleigh damping method was employed to obtain the structural damping matrix.

According to the Canton Tower as an analytical model, the 19th and 38th node layers signify the main tower waist and top, respectively. The HMD control system is located at the 37th node layer. Consequently, the motion equation incorporating the HMD control system can be formulated as

$$\mathbf{M}\ddot{\mathbf{x}} + \mathbf{C}\dot{\mathbf{x}} + \mathbf{K}\mathbf{x} = \boldsymbol{\delta}F_u + \boldsymbol{\partial}\mathbf{F_w} \tag{25}$$

where **M**, **C**, and **K** represent the mass, damping, and stiffness matrices, respectively, with details provided in Appendix A. The vectors $\mathbf{x}$, $\dot{\mathbf{x}}$ and $\ddot{\mathbf{x}}$ correspond to displacement, velocity, and acceleration, respectively. $\boldsymbol{\delta}$ and $\boldsymbol{\partial}$ denote the position vectors for the control force and excitation, respectively. F_u serves as the control force input, while the wind load vector is denoted by $\mathbf{F_w}$.

For succinctness, Eq. (25) is rewritten in the form of a state-space equation, as shown in Eq. (1); where $\mathbf{Z}=\{\mathbf{x},\dot{\mathbf{x}}\}^{\mathrm{T}}$ denotes the state variables, $\mathbf{U}=\{F_u,\mathbf{F_w}\}^{\mathrm{T}}$ is the status input and **Y** represents the status output. The matrices **A, B**, **G** and **D** are expressed as follows

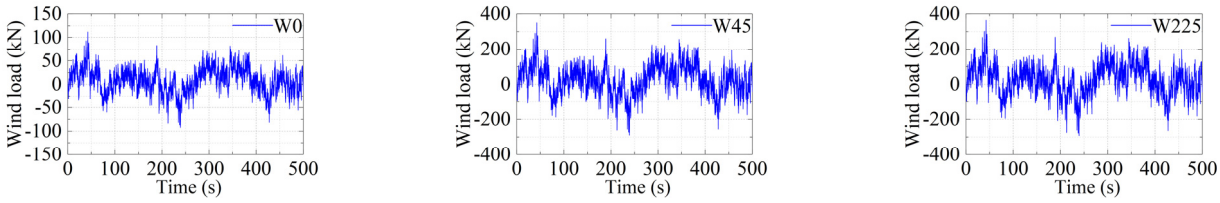

(a) 0° wind attack angle (b) 45° wind attack angle (c) 225° wind attack angle

Fig. 6 10-year-return period wind load time history at different wind attack angles

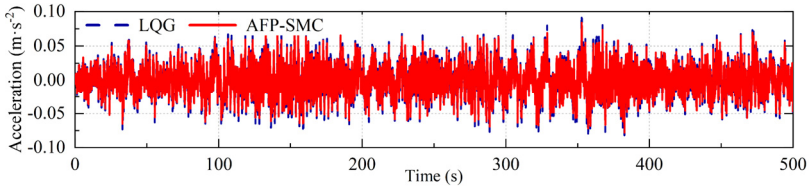

(a) Acceleration

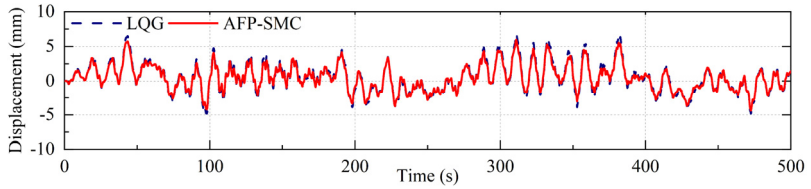

(b) Displacement

Fig. 7 Time history of tower top response under wind load at 0° wind attack angle

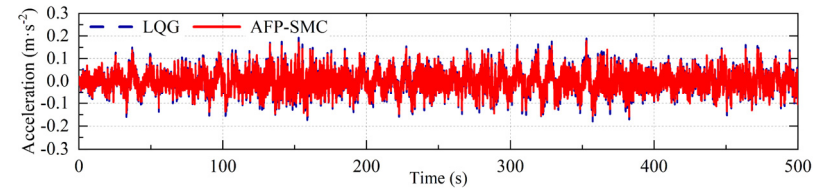

(a) Acceleration

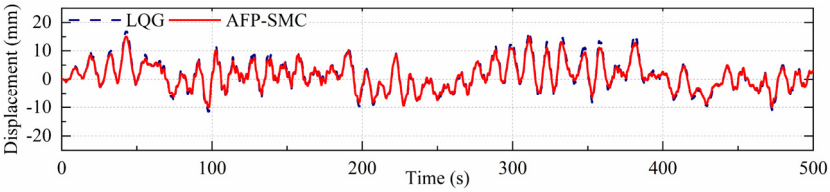

(b) Displacement

Fig. 8 Time history of tower top response under wind load at 45° wind attack angle

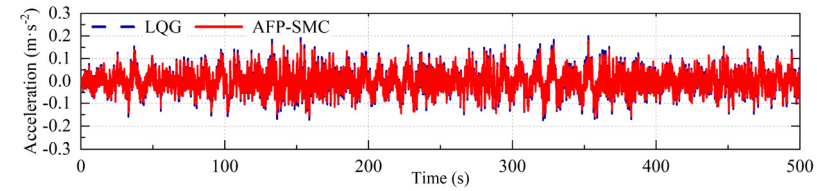

(a) Acceleration

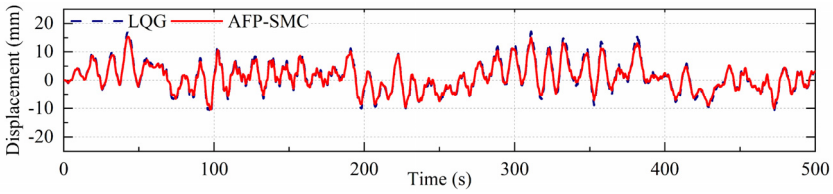

(b) Displacement

Fig. 9 Time history of tower top response under wind load at 225° wind attack angle

$$\mathbf{A} = \begin{bmatrix} \mathbf{0} & \mathbf{I} \\ -\mathbf{M}^{-1}\mathbf{K} & -\mathbf{M}^{-1}\mathbf{C} \end{bmatrix} \tag{26}$$

$$\mathbf{G} = \begin{bmatrix} \mathbf{H} & \mathbf{0} \\ -\mathbf{M}^{-1}\mathbf{K} & -\mathbf{M}^{-1}\mathbf{C} \end{bmatrix} \tag{27}$$

$$\mathbf{B} = \mathbf{D} = \begin{bmatrix} \mathbf{0} & \mathbf{0} \\ \mathbf{M}^{-1}\boldsymbol{\partial} & \mathbf{M}^{-1}\boldsymbol{\delta} \end{bmatrix} \tag{28}$$

where $\mathbf{H}$ is the displacement transformation matrix. The designed objective function (Eq. (15)) and the formulated control force equation (Eq. (24)) are employed to achieve precise control over both the stroke and control force of the HMD.

3.2 Analysis of simulation results

The simulation of the Canton Tower analysis model was carried out in Matlab/Simulink employing the proposed AFP-SMC control algorithm. The structural feedback utilized in this simulation was partial state feedback, augmented with a Kalman filter for state estimation. The weight matrix in Eq. (16) was optimized using a genetic algorithm. The solution was derived using the fourth-order Runge-Kutta method, with a calculation timestep of 0.01 s. For simulation and experimentation, three 10-year return period wind loads with different wind attack angles (0°, 45°, and 225°) were chosen as external loading inputs, as depicted in Fig. 6. The basic wind pressure is 0.26 kN/m^2. An autoregressive model (Samaras *et al*. 1985) was adopted to derive the time history curve of fluctuating wind speed, leading to the generation of wind loadings based on (Iannuzzi and Spinelli 1987).

Figs. 7-9 illustrate the time histories of acceleration and displacement at the tower top of the Canton Tower analysis model, as computed by both AFP-SMC and LQG under various wind loads. The maximum tower top acceleration and displacement values calculated by AFP-SMC are 5.1% and 2.8% smaller, respectively, than those calculated by LQG. Moreover, the time history values for AFP-SMC are generally lesser than the values of LQG. As demonstrated in Figs. 10-11, AFP-SMC excels over LQG in dampening structural vibrations. The illustrations clarify that, at identical elevations, the structural response from AFP-SMC is invariably lesser than that of LQG, a difference that accentuates with height. The results indicate that the proposed AFP-SMC has better control performance than LQG. Additionally, detailed comparative results of structural responses and devices can be found in Tables 2 and 3.

In Table 2, the vibration reduction ratio (VRR) of the maximum displacement of the tower top according to AFP-SMC was 3% higher than that of LQG, and the VRR of the maximum tower waist acceleration according to AFP-SMC was 4% higher than that of LQG. Table 3 displays the TMD

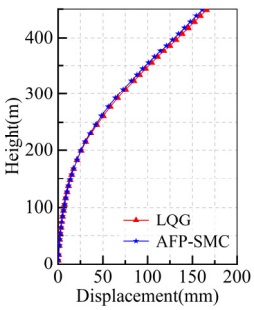

(a) 0° wind attack angle

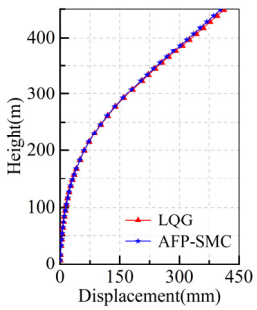

(b) 45° wind attack angle

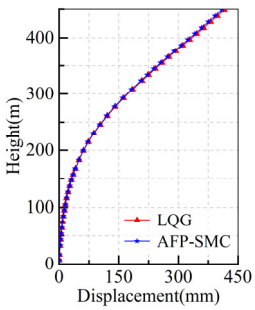

(c) 225° wind attack angle

Fig. 10 Displacement profile of analysis model under different wind loads

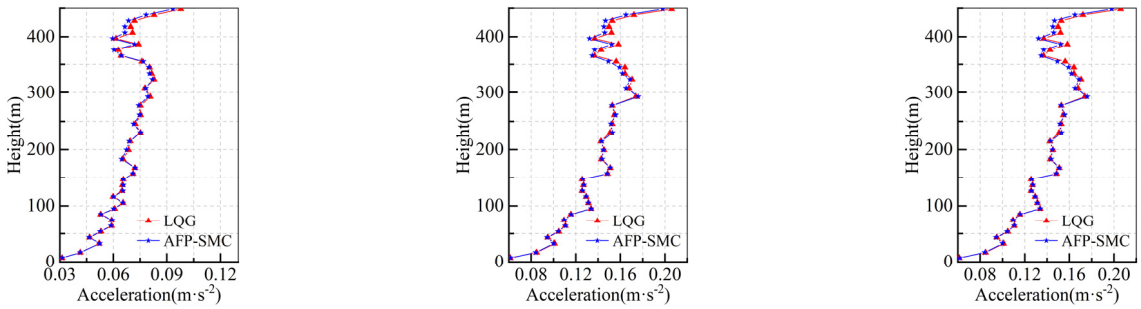

(a) 0° wind attack angle (b) 45° wind attack angle (c) 225° wind attack angle

Fig.11 Acceleration profile of analysis model under different wind loads

Table 2 VRR of structural responses under different wind loads

Wind attack angle		0°		45°		225°	
		LQG	AFP-SMC	LQG	AFP-SMC	LQG	AFP-SMC
Tower Waist	Maximum displacement	38%	41%	44%	45%	44%	45%
	MSE of displacement	45%	46%	48%	49%	48%	49%
	Maximum acceleration	7%	8%	9%	8%	9%	9%
	MSE of acceleration	5%	5%	8%	8%	8%	8%
Tower Top	Maximum displacement	39%	40%	41%	43%	42%	42%
	MSE of displacement	46%	47%	48%	49%	48%	49%
	Maximum acceleration	25%	29%	35%	36%	35%	36%
	MSE of acceleration	36%	37%	44%	44%	44%	45%

*VRR = (1-peak response of controlled structure/peak response of uncontrolled structure)×100%;
MSE: Mean Squared Error

Table 3 Response of TMD and AMD under different wind loads

Wind attack angle	0°		45°		225°	
Item	LQG	AFP-SMC	LQG	AFP-SMC	LQG	AFP-SMC
Stroke of TMD (m)	0.205	0.183	0.449	0.410	0.458	0.419
AMD device stroke (m)	0.350	0.526	0.895	1.180	0.908	1.193
AMD device control force (N)	28752	28175	57143	56567	58573	58438

stroke, AMD stroke, and control force output results for HMD under AFP-SMC and LQG controls. Compared with LQG, AFP-SMC diminishes the stroke of the TMD and AMD control force outputs by a maximum of 0.039 m and 577 N, respectively. Nevertheless, the stroke of the AMD calculated by the AFP-SMC was larger than that of the LQG, with a maximum difference of 0.285 m. It should be noted that even though the AFP-SMC control algorithm augments the stroke of the AMD, it remains within permissible limits. An increase in the stroke of the AMD is beneficial for reducing the stroke of the TMD (Cao and Li 2004). Furthermore, it is worth noting that the AMD in the Canton Tower is affixed at the top of the TMD (refer to Fig. 5(b)), and its dimension is significantly smaller than that of the TMD. Consequently, the limitation of the space for AMD stroke is not the primary concern. Instead, the focus is on the limitation of TMD stroke. Therefore, the priority should be to minimize the working stroke of the TMD to the greatest extent possible.

To further compare the control performance of the two control algorithms, Benchmark evaluation criteria (Spencer *et al*. 1998) described by Eqs. (29)-(33) were used in this study.

1.Structural response evaluation criteria

$$J_1 = \frac{1}{\mathrm{n}} \sum_{i=1}^{\mathrm{n}} \left(1 - \frac{u_{\mathrm{s,i}}}{u_{\mathrm{s,i}}^{\mathrm{u}}}\right) \times 100\% \tag{29}$$

$$J_2 = \frac{1}{\mathrm{n}} \sum_{i=1}^{\mathrm{n}} \left(1 - \frac{a_{\mathrm{s,i}}}{a_{\mathrm{s,i}}^{\mathrm{u}}}\right) \times 100\% \tag{30}$$

where $u_{\mathrm{s,i}}$ and $a_{\mathrm{s,i}}$ are the maximum displacement and maximum absolute acceleration of the i-th node layer of the analytical model with control, respectively; $u_{\mathrm{s,i}}^{\mathrm{u}}$ and $a_{\mathrm{s,i}}^{\mathrm{u}}$ correspond to the responses of the tower without control.

2. AMD device response evaluation criteria

$$J_3 = \max\left\{1 - \frac{u_{\mathrm{T}}}{u_{\mathrm{T,lim}}}\right\} \times 100\% \tag{31}$$

$$J_4 = \max\left\{1 - \frac{u_{\mathrm{A}}}{u_{\mathrm{A,lim}}}\right\} \times 100\% \tag{32}$$

$$J_5 = \max\left\{1 - \frac{F}{F_{\mathrm{lim}}}\right\} \times 100\% \tag{33}$$

where u_{T} and $u_{\mathrm{T,lim}}$ are the TMD stroke and maximum stroke limit, respectively; u_{A} and $u_{\mathrm{A,lim}}$ are the peak stroke and the maximum stroke limit of the AMD respectively. F and F_{lim} denote the peak and maximum output limits of the control force by the AMD, respectively. The $u_{\mathrm{T,lim}}$ and $u_{\mathrm{A,lim}}$ are set to 1.5 m for calculation comparison in this study, and F_{lim} is 72 kN.

Criteria J_1 and J_2 reflect the displacement and acceleration response of the structure; J_3 and J_4 evaluate the control effect of the stroke of the TMD and AMD, respectively; and J_5 evaluates the surplus degree of the control force of AMD. The higher the value of each criterion, the better the control effect.

Table 4 delineates the comparative assessment of the dynamic response control capabilities of the Canton Tower analysis model under the control of AFP-SMC and LQG. Criterion J_2 indicates that AFP-SMC achieved a maximum increase of 2.68% in the acceleration control effect of the entire structure, while criterion J_1 shows that it presented a slight increase in the displacement control effect of the entire structure, with a maximum increase of 1.13%. Additionally, J_3 suggests that the stroke of TMD calculated by AFP-SMC is less than that of LQG, and J_5 indicates that AFP-SMC performs slightly better than LQG in terms of the control force output of AMD. J_4 shows that the stroke of the AMD calculated by AFP-SMC is larger than that of LQG. These evaluative metrics align coherently with the data presented in Tables 2 and 3.

4. Robustness analysis of control algorithm

To further assess the robustness of the AFP-SMC algorithm, the impact of variations in control system parameters on the effectiveness of structural control was analyzed. As depicted in Fig. 5(b), the Canton Tower incorporates TMDs configured as fire water tanks. The TMD mass is inherently variable, depending on the water level, and deviations may also arise in structural stiffness and damping due to construction inconsistencies or other external influences. Furthermore, sensor malfunctions could introduce computational inaccuracies into the control system. Consequently, this investigation considers these sources of interference, including TMD mass variability, structural stiffness and damping discrepancies, and sensor faults, to verify the robustness of the AFP-SMC algorithm.

Table 4 Evaluation criteria results of LQG and AFP-SMC under different wind loads

Criteria	0° wind attack angle		45° wind attack angle		225° wind attack angle	
	LQG	AFP-SMC	LQG	AFP-SMC	LQG	AFP-SMC
J_1(%)	38.30	39.43	42.22	43.01	42.65	43.17
J_2(%)	13.78	15.66	16.26	18.99	16.40	19.08
J_3(%)	86.34	87.78	70.09	72.64	69.50	72.08
J_4(%)	76.65	64.95	40.36	21.36	39.47	20.44
J_5(%)	60.07	60.87	20.63	21.43	18.65	18.84

Table 5 Structural response to mass changes in TMD (0° wind attack angle)

Item	Response	Mass×90%		Mass×80%		Mass×70%	
		AFP-SMC	LQG	AFP-SMC	LQG	AFP-SMC	LQG
Tower top displacement	Peak value (mm)	6.987	7.126	7.398	7.662	7.963	8.313
	VRR (%)	36.76	35.51	33.04	30.65	27.93	24.76
Tower top acceleration	Peak value ($m \cdot s^{-2}$)	0.091	0.095	0.088	0.091	0.089	0.090
	VRR (%)	30.95	27.61	33.17	30.92	32.04	31.13
Tower waist displacement	Peak value (mm)	5.039	5.210	5.488	5.696	5.975	6.373
	VRR (%)	38.95	36.88	33.51	30.99	27.60	22.78
Tower waist acceleration	Peak value ($m \cdot s^{-2}$)	0.069	0.069	0.070	0.069	0.070	0.070
	VRR (%)	7.29	7.40	6.78	7.41	6.28	6.37
Entirety displacement	VRR (%)	32.28	31.71	28.99	27.95	24.91	22.42
Entirety acceleration	VRR (%)	12.60	11.75	12.23	11.35	11.77	10.78
AMD control force	Peak value (N)	25410	27023	25042	25955	23052	26733

Table 6 Structural response to mass changes in TMD (45° wind attack angle)

Item	Response	Mass×90%		Mass×80%		Mass×70%	
		AFP-SMC	LQG	AFP-SMC	LQG	AFP-SMC	LQG
Tower top displacement	Peak value (mm)	17.620	18.190	18.643	19.506	19.699	20.946
	VRR (%)	39.55	37.60	36.05	33.08	32.42	28.15
Tower top acceleration	Peak value ($m \cdot s^{-2}$)	0.197	0.202	0.203	0.207	0.207	0.213
	VRR (%)	36.68	35.29	34.85	33.58	33.69	31.80
Tower waist displacement	Peak value (mm)	12.664	12.911	13.616	14.230	14.729	15.776
	VRR (%)	41.66	40.53	37.28	34.45	32.15	27.33
Tower waist acceleration	Peak value ($m \cdot s^{-2}$)	0.144	0.143	0.145	0.145	0.146	0.147
	VRR (%)	7.94	8.26	7.27	7.15	6.65	6.01
Entirety displacement	VRR (%)	39.96	38.90	36.16	34.25	31.79	28.47
Entirety acceleration	VRR (%)	16.76	16.04	16.08	15.25	15.31	14.43
AMD control force	Peak value (N)	53984	55987	53138	57581	54351	59328

Table 7 Structural response to mass changes in TMD (225° wind attack angle)

Item	Response	Mass×90%		Mass×80%		Mass×70%	
		AFP-SMC	LQG	AFP-SMC	LQG	AFP-SMC	LQG
Tower top displacement	Peak value (mm)	17.674	18.263	18.706	19.593	19.839	21.042
	VRR (%)	40.16	38.16	36.66	33.66	32.83	28.76
Tower top acceleration	Peak value ($m \cdot s^{-2}$)	0.196	0.203	0.202	0.206	0.208	0.216
	VRR (%)	37.70	35.44	35.85	34.57	33.87	31.49
Tower waist displacement	Peak value (mm)	12.671	12.928	13.635	14.289	14.772	15.846
	VRR (%)	42.50	41.33	38.13	35.16	32.96	28.09
Tower waist acceleration	Peak value ($m \cdot s^{-2}$)	0.143	0.142	0.144	0.144	0.145	0.146
	VRR (%)	8.21	8.49	7.52	7.34	6.87	6.18
Entirety displacement	VRR (%)	40.61	39.56	36.86	34.89	32.49	29.14
Entirety acceleration	VRR (%)	16.89	16.12	16.20	15.36	15.45	14.51
AMD control force	Peak value (N)	54957	58311	54131	58947	55633	60775

4.1 Analysis of system response to changes in the mass of TMD

In the designated simulations, the mass of TMD within the HMD was decreased by 10%, 20%, and 30%. Under the influence of three distinct wind load excitations, a comparison between the control performances of AFP-SMC and LQG is presented in Tables 5-7.

Tables 5-7 present a comparison of the control performance of AFP-SMC and LQG on the structure under different TMD masses. For a more intuitive assessment, Fig. 12(a) presents a three-dimensional visualization of VRR differences, calculated as the VRR values of AFP-SMC minus those of LQG, as listed in Tables 5-7. The visualization elucidates that for different TMD mass adjustments, the maximum VRR value under AFP-SMC exceeds that of LQG by differences of 3.34%, 3.0%, and 4.82%. On the other hand, the VRR corresponding to the tower waist acceleration determined by AFP-SMC is slightly less than that determined by LQG, with an average difference of 0.29%. Furthermore, the average control force output of the AMD calculated by AFP-SMC is 7.26% lower than that of LQG. The results show that AFP-SMC has a better control effect and anti-interference ability than LQG.

4.2 System response analysis under structural parameter disturbance

Discrepancies can arise between an actual structure and its ideal finite element model due to uncertainties in building materials and variations in the construction process. Consequently, this study factored in the stiffness and damping of the structure as elements influencing disturbance control efficacy.

Tables 8-9 display the control outcomes for both tower top and tower waist in terms of displacement and acceleration, as determined by AFP-SMC and LQG, when structural stiffness and damping each experienced a 10% reduction. Similarly, for the sake of comparison, a three-SMC and LQG listed in Tables 8-9 are presented in Fig. 12(b). The graph shows that, when the stiffness and damping of the structure were reduced by 10%, the

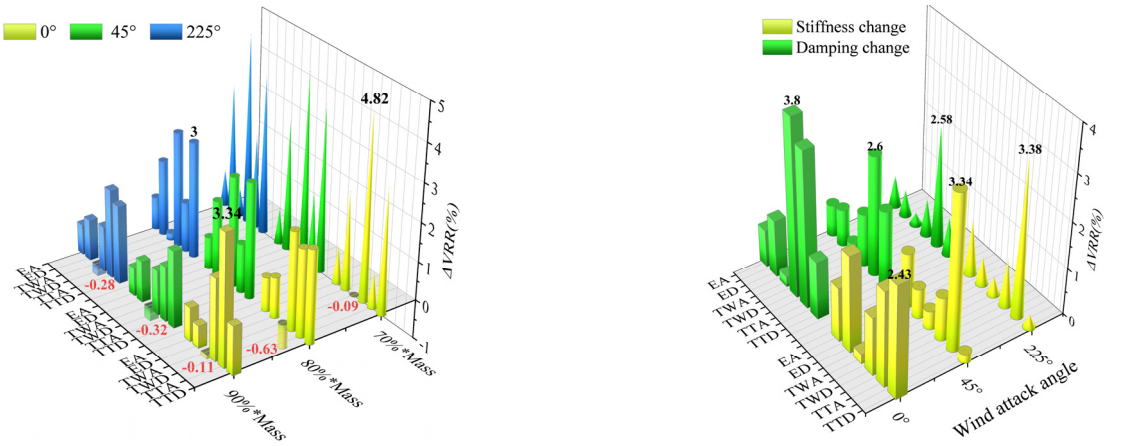

(a) Mass changes in TMD (b) Stiffness and damping changes in structure

Fig. 12 VRR difference between AFP-SMC and LQG

TTD: Tower top displacement; TTA: Tower top acceleration; TWD: Tower waist displacement; TWA: Tower waist acceleration; ED: Entirety displacement; EA: Entirety acceleration.

Table 8 Structural response to structural stiffness changes

Item	Response	Wind attack angle					
		0°		45°		225°	
		AFP-SMC	LQG	AFP-SMC	LQG	AFP-SMC	LQG
Tower top displacement	Peak value (mm)	7.220	7.465	18.800	18.850	19.265	19.335
	VRR (%)	28.70	26.27	27.94	27.74	27.51	27.25
Tower top acceleration	Peak value ($m \cdot s^{-2}$)	0.091	0.091	0.206	0.206	0.269	0.269
	VRR (%)	26.03	23.97	26.64	23.30	25.31	21.93
Tower waist displacement	Peak value (mm)	5.340	5.438	13.663	13.845	13.921	14.121
	VRR (%)	31.00	29.74	29.25	28.31	29.17	28.15
Tower waist acceleration	Peak value ($m \cdot s^{-2}$)	0.080	0.080	0.163	0.163	0.176	0.176
	VRR (%)	5.79	5.57	7.79	7.39	7.97	7.59
Entirety displacement	VRR (%)	24.29	22.21	25.77	25.13	25.47	24.87
Entirety acceleration	VRR (%)	7.84	6.68	9.14	7.95	9.05	7.87
AMD control force	Peak value (N)	35346	33154	72000	72000	72000	72000

dimensional graph of the difference in VRR between AFP-

Table 9 Structural response to structural damping changes

Item	Response	Wind attack angle					
		0°		45°		225°	
		AFP-SMC	LQG	AFP-SMC	LQG	AFP-SMC	LQG
Tower top displacement	Peak value (mm)	6.653	6.794	16.754	17.243	17.063	17.304
	VRR (%)	41.12	39.87	43.82	42.18	43.55	42.75
Tower top acceleration	Peak value ($m \cdot s^{-2}$)	0.097	0.097	0.214	0.214	0.325	0.325
	VRR (%)	28.86	25.52	36.28	33.68	36.16	33.58
Tower waist displacement	Peak value (mm)	4.895	5.214	11.950	12.201	12.197	12.370
	VRR (%)	41.73	37.93	45.99	44.85	45.70	44.93
Tower waist acceleration	Peak value ($m \cdot s^{-2}$)	0.072	0.072	0.150	0.150	0.163	0.163
	VRR (%)	7.78	7.55	8.80	8.52	9.09	8.84
Entirety displacement	VRR (%)	40.09	38.86	43.79	42.99	43.99	43.45
Entirety acceleration	VRR (%)	10.45	9.65	14.64	13.96	14.79	14.12
AMD control force	Peak value (N)	28749	29318	57916	58035	59472	59778

difference in VRR between AFP-SMC and LQG was positive, indicating that the VRR calculated by AFP-SMC was greater than that calculated by LQG. With reduced structural stiffness, the peak VRR differences between AFP-SMC and LQG were 2.43%, 3.34%, and 3.38%. Meanwhile, with reduced structural damping, these differentials were 3.8%, 2.6%, and 2.58%. These results reflect the superior control performance of AFP-SMC over LQG. The AMD control forces from both control algorithms are approximately the same. Nevertheless, when the structural stiffness decreased by 10%, the control forces calculated by both control algorithms reached the limit value, indicating that the influence of structural stiffness changes on both control algorithms is significant.

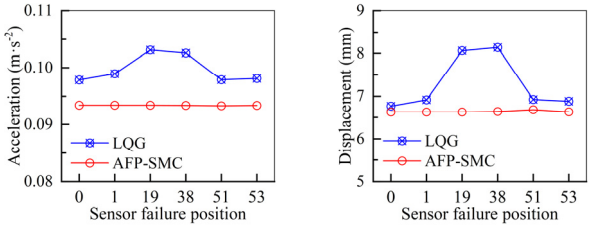

(a) Acceleration (b) Displacement

Fig. 13 Peak tower top responses: 0° wind attack angle

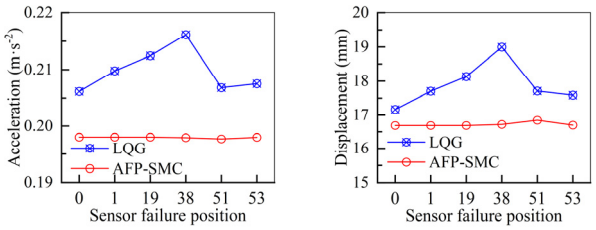

(a) Acceleration (b) Displacement

Fig. 14 Peak tower top responses: 45° wind attack angle

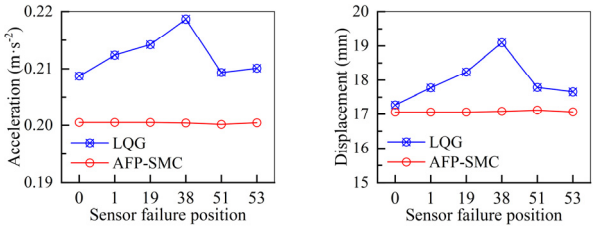

(a) Acceleration (b) Displacement

Fig. 15 Peak tower top responses: 2255° wind attack angle

4.3 System response analysis to sensor failure

The control process necessitates signal feedback from various sensors, including displacement and acceleration sensors, to calculate the control force. A malfunctioning sensor may affect the calculation effect of the controller, potentially leading the system to fall short of its control standards. Therefore, this study analyzed the responses of single acceleration sensor failures at specific structural layers, corresponding to node layers 1, 19, 38, and 51 in the Canton Tower analysis model. In Figs. 13-15, the coordinates 1, 19, 38, and 51 symbolize the first node layer of the main tower, tower waist, tower top, and mast, respectively. The coordinate 0 represents an operational sensor, while coordinate 53 indicates that the position of the sensor is on the HMD.

Figs. 13-15 show the peak responses of the acceleration and displacement of the tower top in case of a single sensor failure under different wind loads. When acceleration sensors at positions 1, 19, and 38 malfunctioned, the computed peak responses by LQG for both acceleration and displacement of the tower top showed a significant increase, and failures of sensors at positions 51 and 53 led to a slight rise in the peak response. In contrast to LQG, the peak responses of the tower top calculated by AFP-SMC were almost unaffected in the case of a single sensor failure. Fig. 16 shows the peak results of the AMD control force when a single sensor failed at different locations under different wind loads. For sensor failures at positions 19 and 38, the AMD control force calculated by LQG increased significantly, reaching the limit of 72 kN, whereas the AMD control force calculated by AFP-SMC increased slightly. These results indicate that the stability and anti-interference ability of AFP-SMC are better than those of the LQG algorithm.

4.4 Practical dynamic characteristics of AMD

The AMD model is typically considered an ideal model in numerical simulations since it ignores the effects of friction and ripple thrust. Canton Tower has two AMDs, each of which is driven by four linear motors (see Fig. 17). In this study, tests are conducted to evaluate the practical dynamic characteristics of the AMD control devices in Canton Tower, and formulas are proposed for calculating the ripple thrust and comprehensive resistance of a single

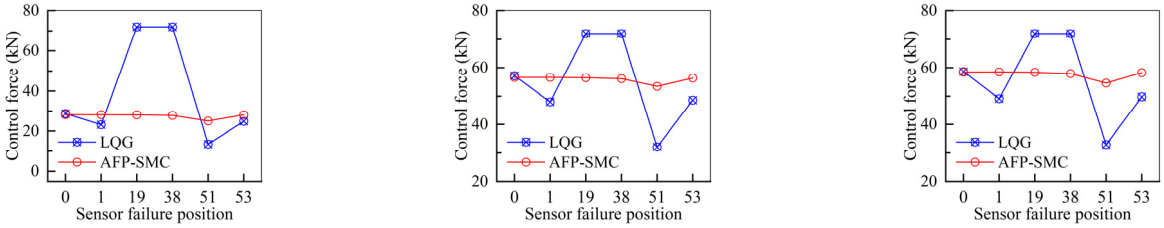

(a) 0° wind attack angle (b) 45° wind attack angle (c) 225° wind attack angle

Fig. 16 AMD control force peak values under sensor failure conditions

Fig. 17 Photograph of AMD in Canton Tower

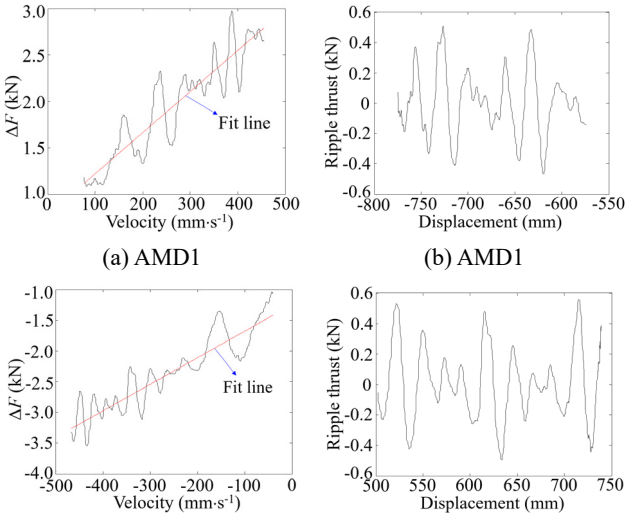

(a) AMD1 (b) AMD1

(c) AMD2 (d) AMD2

Fig. 18 Relationship curves between ΔF and velocity and between ripple thrust and displacement of AMD

AMD driven by multiple linear motors. The stability and control efficiency of the AFP-SMC algorithm were further verified.

4.4.1 Identification of comprehensive resistance and ripple thrust

The difference between the command force and the actual driving force is expressed by ΔF. Under the action of a constant command force of -5.2 kN, the relationship between the ΔF and velocity for the AMD, as well as the correlation between the pulsating thrust and the displacement of the mass block for the AMD are shown in Fig. 18. The red lines in Figs. 18(a) and (c) represent the relationship between the fitted comprehensive resistance and velocity.

The formulas for calculating the comprehensive resistance are as follows

$$F_{k1} = 4349.3x_{a1} + 816.6\mathrm{sgn}(\dot{x}_{a1}) \tag{34}$$

$$F_{k2} = 4441.5x_{a2} + 1045.8\mathrm{sgn}(\dot{x}_{a2}) \tag{35}$$

where F_{k1} and F_{k2} are the comprehensive resistances of AMD1 and AMD2, respectively; x_a and $\dot{x}_a$ are the displacement and velocity of AMD, respectively.

To discern the correlation between ripple thrust and the displacement of the AMD mass block, an analysis was

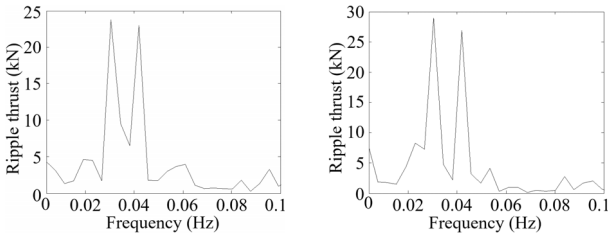

(a) AMD1 subsystem (b) AMD2 subsystem

Fig. 19 Ripple thrust spectra

conducted on the frequency spectra of the ripple thrust. Fig. 19 illustrates the frequency spectra for the ripple thrust in both AMD1 and AMD2 subsystems, subjected to a consistent command force of -5.2 kN.

Based on the spectrum for each case, the primary ripple-thrust frequencies for the AMD1 subsystem were identified as 0.0315, 0.042, and 0.0208 Hz, while the AMD2 subsystem had frequencies of 0.0312, 0.0415, and 0.0208 Hz. Subsequently, the amplitude for each respective frequency was ascertained from the spectrum diagram. Using the correlation curve between ripple thrust and displacement in conjunction with the least squares method, the phase angle for each frequency was established. The resulting ripple thrust, represented as f_{ri}(i = 1, 2), is articulated as follows

$$\begin{aligned} f_{r1} = {} & 189\sin(0.0630\pi x_{a1}(t) + 0.7499) \\ & +182.25\sin(0.840\pi x_{a1}(t + 5.189) \\ & +47.25\sin(0.0416\pi x_{a1}(t + 1.193) \end{aligned} \tag{36}$$

$$\begin{aligned} f_{r2} = {} & 217.5\sin(0.0624\pi x_{a2}(t) + 5.912) \\ & +172.5\sin(0.0830\pi x_{a2}(t + 3.037) \\ & +52.5\sin(0.0416\pi x_{a2}(t) + 1.847) \end{aligned} \tag{37}$$

Fig. 20 shows the fitting results for the ripple thrust in both AMD1 and AMD2 subsystems under the action of a constant command force of -5.2 kN compared with the actual values. The alignment between the derived theoretical formula for ripple thrust and the actual ripple thrust data signifies the efficacy and applicability of the testing methodology in ripple thrust identification.

The fitted comprehensive resistance formula is found to be inadequate in representing the comprehensive resistance of AMD at low velocities. In the case of low velocity, the friction force is deemed equivalent to the maximum value

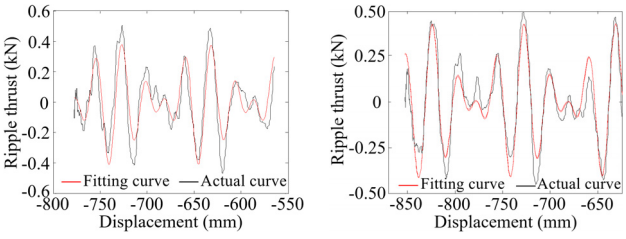

(a) AMD1 subsystem (b) AMD2 subsystem

Fig. 20 Relationship between ripple thrust and position at constant command force (-5.2 kN)

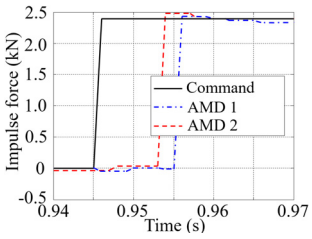

Fig. 21 Time delay for 2.4 kN impulse force

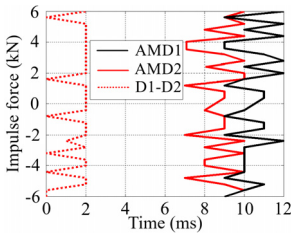

Fig. 22 Time delay for different impulse forces

of the unbalanced force and static resistance. Consequently, the modified formulas for calculating the comprehensive resistance are shown in Eqs. (38)-(39). where D_a denotes the constant velocity determined experimentally, and in this study, its value was determined to be 5 mm/s; F_a represents the command force.

To evaluate the time delay and synchronization between the AMD1 and AMD2 subsystems, a pulse command force was employed. This pulse force had a duration of 500 ms. Fig. 21 depicts the time delay experienced by the AMD1 and AMD2 subsystems when subjected to a pulse command force of 2.4 kN, while Fig. 22 illustrates the time delays for the AMD subsystems under varied impulse forces. The term D1-D2 in Fig. 22 represents the response time difference between the AMD1 and AMD2 subsystems. The subsystems exhibited a maximum time delay of 12 ms. This delay, in comparison to the basic period of 9.9661 s (as determined by theoretical model calculations) for Canton Tower, is negligible. Therefore, the multiple linear motor-driven AMD1 and AMD2 subsystems meet the requirements of the actual control system in terms of time delay.

$$F_{k1}(x_{a1}(t)) = \begin{cases} 4349.3x_{a1}(t) + 816.6\mathrm{sgn}(\dot{x}_{a1}(t)) & |\dot{x}_{a1}| \geq D_a \\ \min(816.6, F_a) & |\dot{x}_{a1}| < D_a \text{ and } F_a > 0 \\ \max(-816.6.8, F_a) & |\dot{x}_{a1}| < D_a \text{ and } F_a < 0 \end{cases} \quad (39)$$

$$F_{k2}(x_{a2}(t)) = \begin{cases} 4441.5x_{a2}(t) + 1045.8\mathrm{sgn}(\dot{x}_{a2}(t)) & |\dot{x}_{a2}| \geq D_a \\ \min(1045.8, F_a) & |\dot{x}_{a2}| < D_a \text{ and } F_a > 0 \\ \max(-1045.8, F_a) & |\dot{x}_{a2}| < D_a \text{ and } F_a < 0 \end{cases} \quad (38)$$

4.4.2 Simulation considering comprehensive resistance and ripple thrust of AMD

Based on the formulas for calculating the comprehensive resistance in Section 4.4.1, the structural response results considering the comprehensive resistance and ripple thrust of the AMD are listed in Table 10. Similarly, for ease of comparison, Fig. 23 visually displays the VRR comparison calculated by the two algorithms. The

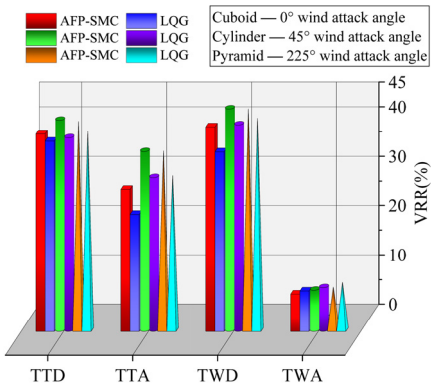

Fig. 23 Structural response in terms of VRR considering comprehensive resistance and ripple thrust of AMD

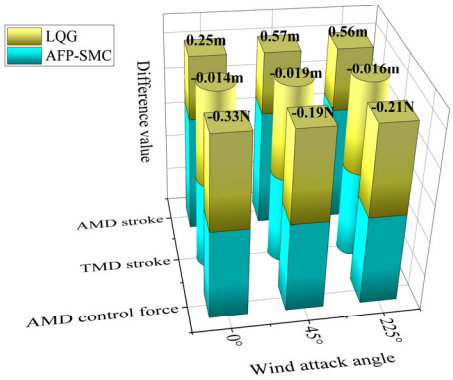

Fig. 24 HMD response considering comprehensive resistance and ripple thrust of AMD

maximum VRR of the tower top displacement, acceleration, and tower waist displacement calculated by AFP-SMC was 3.50%, 5.26%, and 5.01% higher than those derived from the LQG, respectively. Contrarily, the maximum VRR of the tower waist acceleration calculated by AFP-SMC was slightly lower than that of LQG, with an average decrease of 0.71%. Fig. 24 shows the difference in HMD response between AFP-SMC and LQG. The control force output of the AMD and stroke of TMD calculated by AFP-SMC were smaller than those calculated by the LQG control algorithm, resulting in a negative difference. However, the stroke of AMD calculated by AFP-SMC was larger than those calculated by LQG, resulting in a positive difference. The results indicate that the overall control performance of the AFP-SMC algorithm is superior to that of the LQG algorithm.

Table 10 Structural response considering comprehensive resistance and ripple thrust of AMD

Item	Response	Wind attack angle					
		0°		45°		225°	
		AFP-SMC	LQG	AFP-SMC	LQG	AFP-SMC	LQG
Tower top displacement	Peak value (mm)	6.63	6.78	16.67	17.68	17.07	17.67
	VRR (%)	40.04	38.6	42.75	39.25	42.22	40.19
Tower top acceleration	Peak value ($m \cdot s^{-2}$)	0.093	0.101	0.198	0.215	0.201	0.216
	VRR (%)	28.85	23.68	36.47	31.21	36.27	31.31
Tower waist displacement	Peak value (mm)	4.83	5.245	11.93	12.63	12.17	12.59
	VRR (%)	41.43	36.42	45.05	41.83	44.75	42.86
Tower waist acceleration	Peak value ($m \cdot s^{-2}$)	0.069	0.0686	0.143	0.142	0.142	0.140
	VRR (%)	7.56	8.19	8.33	8.85	8.62	9.61
Entirety displacement	VRR (%)	28384	28718	57314	57505	58739	58952
Entirety acceleration	VRR (%)	0.536	0.287	1.180	0.613	1.194	0.635
AMD control force	Peak value (N)	0.183	0.197	0.396	0.412	0.40	0.419

5. Conclusions

This study proposes an AFP-SMC algorithm and conducts a comparative analysis with the LQG control algorithm, utilizing the analytical model of the Canton Tower equipped with HMDs control system. The robustness of AFP-SMC under different interference conditions was compared and analyzed, and formulas for the friction and ripple thrust of the AMD subsystem in Canton Tower were proposed to further verify the robustness of AFP-SMC. The main conclusions are as follows:

- The displacement and acceleration control effect of the tower top and waist, as well as the overall control effect of the analysis model, are better when calculated using AFP-SMC than when using LQG, based on the Canton Tower analysis model under different wind loads. In the HMD control system, the control effect of AFP-SMC on the AMD control force output and TMD stroke is also better than that of LQG. However, the operating stroke of the AMD device is increased by AFP-SMC.
- In the presence of disturbances to the control device and structural parameters, the amplitude change in the structural response under AFP-SMC control is smaller than that of LQG, and the overall control effect of AFP-SMC is better than that of LQG. Furthermore, the influence of structural stiffness changes on both control algorithms is significant. In the case of partial sensor failure, the peak values of the tower top response and AMD control force calculated by AFP-SMC change little, whereas the values calculated by LQG change significantly, even reaching their limits.
- The proposed formulas for the integrated resistance and ripple thrust of the AMD subsystem are further used to verify the stability and reliability of AFP-SMC, based on the results of the tests conducted on the AMD in the Canton Tower analysis model. The simulation results show that, compared with LQG, the control effect of Canton Tower calculated by AFP-SMC is better, and the control force output of AMD and operating stroke of TMD are reduced, but the stroke of AMD is increased.

Acknowledgments

The research described in this paper was financially supported by the Natural Science Foundation of Guangdong Province of China (No. 2021A1515010586), National Natural Science Foundation of China (52378293), National Key R&D Project of China (No. 2021YFE0112200).

References

Alli, H. and Yakut, O. (2005), "Fuzzy sliding-mode control of structures", *Eng. Struct.*, **27**(2), 277-284. https://doi.org/10.1016/j.engstruct.2004.10.007

Baghaei, K.A., Ghaffarzadeh. H., Hadigheh, S.A. and Dias-da-Costa, D. (2019), "Chattering-free sliding mode control with a fuzzy model for structural applications", *Struct. Eng. Mech., Int. J.*, **69**(3), 307-315. https://doi.org/10.12989/sem.2019.69.3.307

Cao, H. and Li, Q.S. (2004), "New control strategies for active tuned mass damper systems", *Comput. Struct.*, **82**(27), 2341-2350. https://doi.org/10.1016/j.compstruc.2004.05.010

Concha, A., Thenozhi, S., Betancourt, R.J. and Gadi, S.K. (2021), "A tuning algorithm for a sliding mode controller of buildings with ATMD", *Mech. Syst. Signal Pr.*, **154**, 107539. https://doi.org/10.1016/j.ymssp.2020.107539

Esteki, K., Bagchi, A. and Sedaghati, R. (2015), "Semi-active control of seismic response of a building using MR fluid-based tuned mass damper", *Smart Struct. Syst., Int. J.*, **16**(5), 807-833. https://doi.org/10.12989/sss.2015.16.5.807

Fallah, A.Y. and Taghikhany, T. (2015), "Sliding mode fault detection and fault-tolerant control of smart dampers in semi-active control of building structures", *Smart Mater. Struct.*, **24**(12), 125030. https://doi.org/10.1088/0964-1726/24/12/125030

Ghaffarzadeh, H. and Aghabalaei, K. (2017), "Adaptive fuzzy sliding mode control of seismically excited structures", *Smart Struct. Syst., Int. J.*, **19**(5), 577-585.

https://doi.org/10.12989/sss.2017.19.5.577
Ho, C.C. and Ma, C.K. (2007), "Active vibration control of structural systems by a combination of the linear quadratic Gaussian and input estimation approaches", *J. Sound Vib.*, **301**(3-5), 429-449. https://doi.org/10.1016/j.jsv.2005.12.061
Iannuzzi, A. and Spinelli, P. (1987), "Artificial wind generation and structural response", *J. Struct. Eng.*, **113**(12), 2382-2398. https://doi.org/10.1061/(ASCE)0733-9445(1987)113:12(2382)
Khansefid, A. and Bakhshi, A. (2019), "Advanced two-step integrated optimization of actively controlled nonlinear structure under mainshock-aftershock sequences", *J. Vib. Control*, **25**(4), 748-762. https://doi.org/10.1177/107754631879553
Koutsoloukas, L., Nikitas, N. and Aristidou, P. (2022), "Passive, semi-active, active and hybrid mass dampers: A literature review with associated applications on building-like structures", *Develop. Built Environ.*, 100094. https://doi.org/10.1016/j.dibe.2022.100094
Kumar, G., Kumar, R. and Kumar, A. (2023), "A Review of the Controllers for Structural Control", *Arch. Computat. Methods Eng.*, **30**, 3977-4000. https://doi.org/10.1007/s11831-023-09931-y
Mamat, N., Yakub, F., Salim, S., Ali, M. and Putra, S. (2018), "Analysis of Implementation Control Device in Hybrid Mass Damper System", In: *2018 IEEE International Conference on Automatic Control and Intelligent Systems* (*I2CACIS 2018*), Shah Alam, Malaysia, October. https://doi.org/10.1109/I2CACIS.2018.8603683
Miyamoto, K., Sato, D. and She, J. (2018), "A new performance index of LQR for combination of passive base isolation and active structural control", *Eng. Struct.*, **157**(2018), 280-299. https://doi.org/10.1016/j.engstruct.2017.11.070
Nagashima, I., Maseki, R., Asami, Y., Hirai, J. and Abiru, H. (2001), "Performance of hybrid mass damper system applied to a 36-storey high-rise building", *Earthq. Eng. Struct. Dyn.*, **30**(11), 1615-1637. https://doi.org/10.1002/eqe.84
Nishitani, A. (1998), "Application of active structural control in Japan", *Prog. Struct. Eng. Mater.*, **1**(3), 301-307. https://doi.org/10.1002/pse.2260010312
Ohtori, Y., Christenson, R.E., Spencer Jr, B.F. and Dyke, S.J. (2004), "Benchmark Control Problems for Seismically Excited Nonlinear Buildings", *J. Eng. Mech.*, **130**(4), 366-385. https://doi.org/10.1061/(ASCE)0733-9399(2004)130:4(366)
Rana, R. and Soong, T.T. (1998), "Parametric study and simplified design of tuned mass dampers", *Eng. Struct.*, **20**(3), 193-204. https://doi.org/10.1016/S0141-0296(97)00078-3
Sakamoto, M. and Kobori, T. (1995), "Research, development and practical applications on structural response control of buildings", *Smart Mater. Struct.*, **4**(1A), A58. https://doi.org/110.1088/0964-1726/4/1A/008
Samaras, E., Shinzuka, M. and Tsurui, A. (1985), "ARMA representation of random processes", *J. Eng. Mech.*, **111**(3), 449-461. https://doi.org/10.1061/(ASCE)0733-9399(1985)111:3(449)
Shi, Y., Becker, T.C., Furukawa, S., Sato, E. and Nakashima, M. (2014), "LQR control with frequency-dependent scheduled gain for a semi-active floor isolation system", *Earthq. Eng. Struct. Dyn.*, **43**(9), 1265-1284. https://doi.org/10.1002/eqe.2352
Sladek, J.R. and Klinger, R.E. (1983), "Effect of tuned mass dampers on seismic response", *J. Struct. Eng.*, **109**(8), 2004-2009. https://doi.org/10.1061/(ASCE)0733-9445(1983)109:8(2004)
Spencer, Jr. B.F., Dyke, S.J. and Deoskar, H.S. (1998), "Benchmark problems in structural control: part I—active mass driver system", *Earthq. Eng. Struct. Dyn.*, **27**(11), 1127-1139. https://doi.org/10.1002/(SICI)1096-9845(1998110)27:11<1127::AID-EQE774>3.0.CO;2-F
Thenozhi, S. and Yu, W. (2013), "Advances in modeling and vibration control of building structures", *Annu. Rev. Control*, **37**(2), 346-364. https://doi.org/10.1016/j.arcontrol.2013.09.012
Wu, J.C. and Yang, J.N. (2000), "LQG control of lateral–torsional motion of Nanjing TV transmission tower", *Earthq. Eng. Struct. Dyn.*, **29**(8), 1111-1130. https://doi.org/10.1002/1096-9845(200008)29:83.0.CO;2-R
Xiao H., Zhao D., Gao S. and Spurgeon, S.K. (2022), "Sliding mode predictive control: A survey", *Annu. Rev. Control*, **54**, 148-166. https://doi.org/10.1016/j.arcontrol.2022.07.003
Yakut, O. and Alli, H. (2011), "Neural based sliding mode control with moving sliding surface for the seismic isolation of structures", *J. Vib. Control*, **17**(14), 2103-2113. https://doi.org/10.1177/1077546310395964
Yamamoto, M. and Sone, T. (2014), "Behavior of active mass damper (AMD) installed in high-rise building during 2011 earthquake off Pacific coast of Tohoku and verification of regenerating system of AMD based on monitoring", *Struct. Control Hlth.*, **21**(4), 634-647. https://doi.org/10.1002/stc.1590
Yang, J.N., Wu, J.C. and Agrawal, A.K. (1995), "Sliding mode control for seismically excited linear structures", *J. Eng. Mech.*, **121**(12), 1386-1390. https://doi.org/10.1061/(ASCE)0733-9399(1995)121:12(1386)
You, K.P., You, J.Y. and Kim, Y.M. (2014), "LQG control of along-wind response of a tall building with an ATMD", *Mathe. Probl. Eng.*, **2014**(9). https://doi.org/10.1155/2014/206786
Zuo, H., Bi, K. and Hao, H. (2020), "Simultaneous out-of-plane and in-plane vibration mitigations of offshore monopile wind turbines by tuned mass dampers", *Smart Struct. Syst., Int. J.*, **26**(4), 435-449. https://doi.org/10.12989/sss.2020.26.4.435

Appendix A

Mass, stiffness and damping matrix in Eq. (25).

$$\mathbf{M} = \begin{bmatrix} \boldsymbol{M}_s & \square & \square \\ \square & m_t & \square \\ \square & \square & m_{amd} \end{bmatrix} \tag{A1}$$

$$\mathbf{C} = \begin{bmatrix} \boldsymbol{C}_s + c_t^{(i,i)} & -c_t^{(i,n+1)} & \square \\ -c_t^{(n+1,i)} & c_t + c_{amd} & -c_{amd} \\ 0 & -c_{amd} & c_{amd} \end{bmatrix} \tag{A2}$$

$$\mathbf{K} = \begin{bmatrix} \boldsymbol{K}_s + k_t^{(i,i)} & -k_t^{(i,n+1)} & \square \\ -k_t^{(n+1,i)} & k_t + k_{amd} & -k_{amd} \\ \square & -k_{amd} & k_{amd} \end{bmatrix} \tag{A3}$$

where $\boldsymbol{M}_s$, $\boldsymbol{C}_s$ and $\boldsymbol{K}_s$ respectively denote the mass, stiffness, and damping matrices of the structure, while m_t, c_t and k_t signify the mass, damping, and stiffness parameters for the TMD. For the AMD, the corresponding parameters are represented by m_{amd}, c_{amd} and k_{amd}. It should be noted that, in practice, the damping and stiffness of the AMD are generally not considered. To satisfy the requirements for simulating calculation, c_{amd} and k_{amd} are set to be 0.001. Superscripts (i, i), (i, n+1) and (n+1, i) indicate the row and column positions of specific elements within the matrices. For instance, $c_t^{(i,i)}$ refers to the element of c_t located at the i-th row and i-th column. The expression $C_s + c_t^{(i,i)}$ implies that $c_t^{(i,i)}$ is added to the corresponding element in the C_s matrix.